China Ocean Eng., 2020, Vol. 34, No. 1, P. 56–68
DOI: https://doi.org/10.1007/s13344-020-0006-8, ISSN 0890-5487
http://www.chinaoceanengin.cn/ E-mail: coe@nhri.cn

An Efficient Tide-Surge Interaction Model for the Coast of Bangladesh

M. Mizanur RAHMAN[a], Gour Chandra PAUL[b,*], Ashabul HOQUE[b]

[a]Department of Mathematics, Shahjalal University of Science & Technology, Sylhet 3114, Bangladesh

[b]Department of Mathematics, University of Rajshahi, Rajshahi-6205, Bangladesh

Received January 12, 2019; revised August 1, 2019; accepted September 2, 2019

Abstract

The numerical method of lines (MOLs) in coordination with the classical fourth-order Runge–Kutta (RK(4, 4)) method is used to solve shallow water equations (SWEs) for foreseeing water levels owing to the nonlinear interaction of tide and surge accompanying with a storm along the coast of Bangladesh. The SWEs are developed by extending the body forces with tide generating forces (TGFs). Spatial variables of the SWEs along with the boundary conditions are approximated by means of finite difference technique on an Arakawa C-grid to attain a system of ordinary differential equations (ODEs) of initial valued in time, which are being solved with the aid of the RK(4, 4) method. Nested grid technique is adopted to solve coastal complexities closely with least computational cost. A stable tidal solution in the region of our choice is produced by applying the tidal forcing with the major tidal constituent M_2 (lunar semi-diurnal) along the southern open-sea boundary of the outer scheme. Numerical experimentations are carried out to simulate water levels generated by the cyclonic storm AILA along the coast of Bangladesh. The model simulated results are found to be in a reasonable agreement with the limited available reported data and observations.

Key words: Bangladesh coast, shallow water equations, method of lines, tide-surge interaction, islands, tide generating forces, inverse barometer

Citation: Rahman, M. M., Paul, G. C., Hoque, A., 2020. An efficient tide-surge interaction model for the coast of Bangladesh. China Ocean Eng., 34(1): 56–68, doi: https://doi.org/10.1007/s13344-020-0006-8

1 Introduction

The coastal region of Bangladesh is often lashed by tropical cyclones and accompanying surges causing a considerable loss of life in addition to destruction of belongings. It is found that the major damage is caused by the associated surge rather than by the storm itself (Rahman et al., 2013). An accurate forecast of the tidal surges can mitigate the sufferings of the people along the coastal belt which can best be done through an optimal numerical model (Paul et al., 2017). A considerable amount of investigations on numerical modeling of storm surges have been conducted in the Bay of Bengal (BOB) region including the coast of Bangladesh (see e.g., Johns and Ali, 1980; Roy, 1995; Roy et al., 1999; Debsarma, 2009; Rahman et al., 2011, 2013, 2017; Paul and Ismail, 2012, 2013; Paul et al., 2014, 2016, 2017, 2018a, 2018b). All of the above studies except Paul et al. (2014, 2018a, 2018b) were conducted employing the finite difference method (FDM). Paul et al. (2014, 2018a, 2018b) in their investigations found the MOLs to be suitable over the FDM with regard to stability, accuracy and the central processing unit (CPU) time. It can be noted here that in simulating Indonesian tsunami, 2004 along the coast of Peninsular Malaysia and that of Thailand, Ismail et al. (2007) adopted firstly the MOLs technique to solve the SWEs and found the MOLs to be a suitable procedure over the FDM for analyzing long waves originated in shallow water. In the MOLs technique, a partial differential equation (PDE) or a system of PDEs is transformed into a system of initial value problem (IVP) as a result of spatial discretization. The resulting system of IVP is then integrated over time as an independent variable using any sophisticated ODE solver. The MOLs thus can take the load of the discretizations of time. Further, with the use of a sophisticated time integrator, time step can be chosen in such a process that maintains the stability and accuracy of the emanated solution (Oymak and Selçuk, 1993). The most significant benefit of using the MOLs technique is that it has the easiness of using explicit methods as well as the advantage of stability of the implicit ones except that a poor numerical technique is adopted for solving the evolved IVPs (Selçuk et al., 2002). Thus, it is revealed that there is a facility of adopting any well-developed time integrator for solving the evolved ODEs attained via the practical and convenient technique, the MOLs. Again, the employment of a sophisticated time integrator implies that a desired order of accuracy and computational efficiency can be attained in time in-

*Corresponding author. E-mail: pcgour2001@yahoo.com

tegration devoid of adopting smaller steps of time (Erşahin et al., 2004). Based on the notion, Paul et al. (2018a, 2018b) used the embedded RKARMS(4, 4) method for solving the system of ODEs obtained by the MOLs approach in SWEs. In both the investigations, it was found that the efficiency of the MOLs approach can be increased with the aid of embedded RKARMS(4, 4) method, in which there is an advantage of step size selection, which leads to the error control, as desired in each step, which in turn can generate results with a considerable accuracy as well as minimize computational cost. In spite of all the advantages mentioned above provided by the MOLs, the studies of storm surge problems using the approach are limited, specifically along the Bangladesh coast, which is well-recognized as the world most vulnerable region. The shape of the Bangladesh coastline and its structure, thickly populated low lying islands of different shapes and shallow bathymetry, the mammoth discharge through the Meghna and other rivers, a high tidal range, low lying coastal areas make it a world most vulnerable region for high surge even with a less powerful storm (As-Salek and Yasuda, 2001; Paul and Ismail, 2013). Thus, this region should be investigated significantly. But in order to describe the physics of storm surges properly for a region, specially designed for the coast of Bangladesh, the model must resolve topography of the coast, bathymetry and tidal elevations with a considerable accuracy. A series of studies can be found to conduct for solving the first two problems (Paul and Ismail, 2012, 2013; Paul et al., 2016, 2017, 2018a, 2018b; Rahman et al., 2017). But the third problem has not been paid much attention. It is known from the literature point of view that numerical treatment of tides in coastal seas, application of tidal forcing along the open boundaries of a model domain is sufficient for producing a proper tidal condition (Vatvani et al., 2000). But, for models of larger seashore with sections of deep-ocean or large closed basins, the influence of the tide generating forces (TGFs) on the motion of water can no longer be ignored (see Vatvani et al., 2000; Rahman et al., 2017). Rahman et al. (2017) introduced the TGFs in their investigation conducted with FDM, where the effect of inverse barometer (IB) was not taken into account.

In our present study, the MOLs in addition to the RK(4, 4) method is adopted for solving the developed SWEs owing to the non-linear interaction between tide and surge associated with a storm. The body forces here are extended with TGFs to increase the accuracy in representing tide. The body forces are also extended with pressure gradient force considering the effect of IB. The emphasis is given on the TGFs to show its effect on water levels due to tides and the dynamical interaction of tides with storm surges in the region of our choice. It is also our intention to show by what means our computed results become comparable with the results obtained through some different significant approaches.

2 Mathematical foundation

2.1 Basic dynamical equations

Assuming the curvature of the surface of the earth to be zero, the model is formulated in Cartesian coordinates, which consists of continuity equation to ensure the mass conservation (Eq. (1)) and momentum equations describing the fluid motion in x-direction (Eq. (2)) and y-direction (Eq. (3)) (Rahman et al., 2017):

$$\frac{\partial \zeta}{\partial t}+\frac{\partial}{\partial x}[(\zeta+h)u]+\frac{\partial}{\partial y}[(\zeta+h)v]=0; \tag{1}$$

$$\frac{\partial u}{\partial t}=-u\frac{\partial u}{\partial x}-v\frac{\partial u}{\partial y}+fv-g\frac{\partial \zeta}{\partial x}-\frac{\partial \Omega}{\partial x}-\frac{1}{\rho}\frac{\partial p_{\mathrm{a}}}{\partial x}+\frac{T_x}{\rho(\zeta+h)}-\frac{C_{\mathrm{f}}u(u^2+v^2)^{1/2}}{(\zeta+h)}; \tag{2}$$

$$\frac{\partial v}{\partial t}=-u\frac{\partial v}{\partial x}-v\frac{\partial v}{\partial y}-fu-g\frac{\partial \zeta}{\partial y}-\frac{\partial \Omega}{\partial y}-\frac{1}{\rho}\frac{\partial p_{\mathrm{a}}}{\partial y}+\frac{T_y}{\rho(\zeta+h)}-\frac{C_{\mathrm{f}}v(u^2+v^2)^{1/2}}{(\zeta+h)}. \tag{3}$$

In the above equations, x: southwards in the Cartesian coordinate system; y: eastwards in the Cartesian coordinate system; u, v: vertically integrated Reynold's averaged velocity components in x and y directions, respectively; $\zeta(x,y,t)$: elevation of water from the mean sea level (MSL); $h(x,y)$: ocean depth from the MSL; $\zeta+h$: instantaneous total depth of water column; p_{a} : atmospheric pressure on the sea surface; f: Coriolis parameter; g: local gravitational acceleration; T_x and T_y: wind stress components in x and y directions, respectively; C_{f}: bottom friction coefficient; ρ: sea water density (1023 kg/m^3); Ω : tide generating potential (TGP).

As in Pugh (1987), the TGP yields the equilibrium surface elevation (ESL), η, which is given by

$$\eta=-\frac{\Omega}{g}, \tag{4}$$

wherein, according to Schwiderski (1980),

$$\eta=\sum_{i=0}\eta_i(\varphi,\lambda,t). \tag{5}$$

The ESL is related to the following major species of harmonic tidal constituents (Pugh, 1987):

Semi-diurnal equilibrium tides (ETs):

$$i=2,\ \eta=a\cos^2\varphi\cos(\omega t+\kappa+2\lambda). \tag{6}$$

Diurnal ETs:

$$i=1,\ \eta=a\sin 2\varphi\cos(\omega t+\kappa+\lambda). \tag{7}$$

Long-period ETs:

$$i=0,\ \eta=a(3\cos^3 a/2-1)\cos(\omega t+\kappa). \tag{8}$$

In Eqs. (6)–(8), a characterizes the amplitude and ω the frequency of a constituent, φ and λ represent latitude and east longitude of a desired position, respectively, and κ characterizes astronomical argument. The values of the

parameters involved in Eqs. (6)–(8) for major constituents are obtainable from Schwiderski (1980).

2.2 Boundary conditions

At the mainland and island boundaries, no-slip condition is used. Such a condition is implemented by yielding a zero value to the normal components of the mean current to the mainland as well as island boundaries (Loy et al., 2014). This can simply be attained by representing the boundaries through proper stair steps. It is mentionable at this juncture that such a slip-condition is not flawlessly perfect for forecasting coastal flooding, but it is not critical in the case of storm surge modeling. However, for all the open boundaries, radiation boundary conditions (RBCs) are generally used. These types of conditions permit the outward propagation of energy (wave energy) from the analysis area through the boundaries without reflecting waves (Loy et al., 2014). The RBCs also allow to communicate with the tides of the BOB coming towards the coast of Bangladesh. The following RBCs here are prescribed at the west, east and south open boundaries, respectively (see Rahman et al., 2017):

$$v+\left(\frac{g}{h}\right)^{1/2}\zeta=0; \tag{9}$$

$$v-\left(\frac{g}{h}\right)^{1/2}\zeta=0; \tag{10}$$

$$u-(g/h)^{1/2}\zeta=-2(g/h)^{1/2}a\sin(2\pi t/T+\varphi). \tag{11}$$

In Eq. (11), the parameters a, T and φ represent the amplitude, period and phase associated with the tidal constituent under consideration, respectively.

2.3 Generation of wind stress

In our investigation, the surface stresses are parameterized by (Johns and Ali, 1980)

$$T_x=C_{\mathrm{D}}\rho_{\mathrm{a}}u_{\mathrm{a}}(u_{\mathrm{a}}^2+v_{\mathrm{a}}^2)^{1/2}$$

and $T_y=C_{\mathrm{D}}\rho_{\mathrm{a}}v_{\mathrm{a}}(u_{\mathrm{a}}^2+v_{\mathrm{a}}^2)^{1/2}$,

where u_{a} and v_{a} are the respective x- and y- components of the surface wind velocity at 10 m from the MSL, ρ_{a} ($=0.00129\times10^3\,\mathrm{kg/m^3}$) stands for air density and C_{D} is the surface drag coefficient. It is found that C_{D} varies with wind speed and atmospheric stability (see e.g., Powell et al., 2003). However, in most investigations, it is found to use a uniform value of 2.8×10^{-3} for C_{D} (Das, 1994). Accordingly, in our study, we use the constant value 2.8×10^{-3} for C_{D} throughout.

For the surface wind field over the model domain, we have adopted an idealized formula suggested by Jelesnianski (1965), which is given by

$$V_{\mathrm{a}}=\begin{cases}V_0\sqrt{(r_{\mathrm{a}}/R)^3} & \text{for } r_{\mathrm{a}}\leqslant R\\ V_0\sqrt{R/r_{\mathrm{a}}} & \text{for } r_{\mathrm{a}}>R\end{cases} \tag{12}$$

In Eq. (12), V_0 symbolizes the highest wind speed, r_{a} indicates any radial distance measured from the storm centre and R is the radial distance at which the wind attains its maximum speed. The values of V_0 and R during a cyclonic storm for the domain of our choice are obtainable from Bangladesh Meteorological Department (BMD).

2.4 Pressure field generation

In our study, the components of forcing due to barotropic changes, $\partial p_{\mathrm{a}}/\partial x$ and $\partial p_{\mathrm{a}}/\partial y$ are calculated following Vickery et al. (2000) from the following relation:

$$p_{\mathrm{a}}(r_{\mathrm{a}})=p_0+\Delta p\exp\left[-(R/r_{\mathrm{a}})^{H_0}\right]. \tag{13}$$

From Eq. (13), it is easy to generate $\partial p_{\mathrm{a}}/\partial x$ and $\partial p_{\mathrm{a}}/\partial y$ as:

$$\frac{\partial p_{\mathrm{a}}}{\partial x}=\frac{x-x_{\mathrm{c}}}{r_{\mathrm{a}}}\frac{R\Delta p_{\mathrm{a}}H_0}{r_{\mathrm{a}}^2}\exp\left[-(R/r_{\mathrm{a}})^{H_0}\right]; \tag{14}$$

$$\frac{\partial p_{\mathrm{a}}}{\partial y}=\frac{y-y_{\mathrm{c}}}{r_{\mathrm{a}}}\frac{R\Delta p_{\mathrm{a}}H_0}{r_{\mathrm{a}}^2}\exp\left[-(R/r_{\mathrm{a}})^{H_0}\right], \tag{15}$$

where $r_{\mathrm{a}}=\sqrt{(x-x_{\mathrm{c}})^2+(y-y_{\mathrm{c}})^2}$; $(x_{\mathrm{c}},y_{\mathrm{c}})$ represents the storm's center.

In Eqs. (13)–(15), H_0 is the Holland's radial pressure profile parameter wherein H_0 lies between 1 and 2.5 (see Holland, 1980), where in our investigation, the value of H_0 is set to 2.00; ΔP_{a} is the central pressure deficit and R is the maximum wind radius.

3 Numerical procedure

3.1 Set-up of nested schemes

With the intention of estimating water levels reasonably associated with a storm, the domain must be considerably large to move the storm over the domain at least for 48 hours before hitting the coast (Rahman et al., 2017). Again, with the purpose of incorporating complex land-sea interface (see Fig. 1), the thickly populated small and big offshore islands accurately via stair step method, and to take bathymetric representation properly, a higher spatial resolution is required. But the use of such a high spatial resolution throughout the model domain may invite a huge amount of computational grids which, in turn, requires a smaller time step to ensure CFL (Courant–Friedrichs–Lewy) stability criterion. Both the mentioned facts lead to an increase in computing cost. Bearing in mind the mentioned facts, first a scheme with considerably high spatial resolution referred to as fine mesh scheme (FMS) capable of exercising the major islands of the domain with a considerable accuracy is nested inside a scheme covering up to 15°N latitude in the BOB, which is referred to as coarse mesh scheme (CMS). Further, with the aim of incorporating the said complexities of our region of concern very closely, the region between Patuakhali and Chittagong (see Fig. 1), a scheme with very fine spatial resolution, referred to as very fine mesh scheme (VFMS) is again nested inside the FMS. An essence for clear understanding of the schemes is presented in Table 1 as well as in Fig. 1. Coupling of the

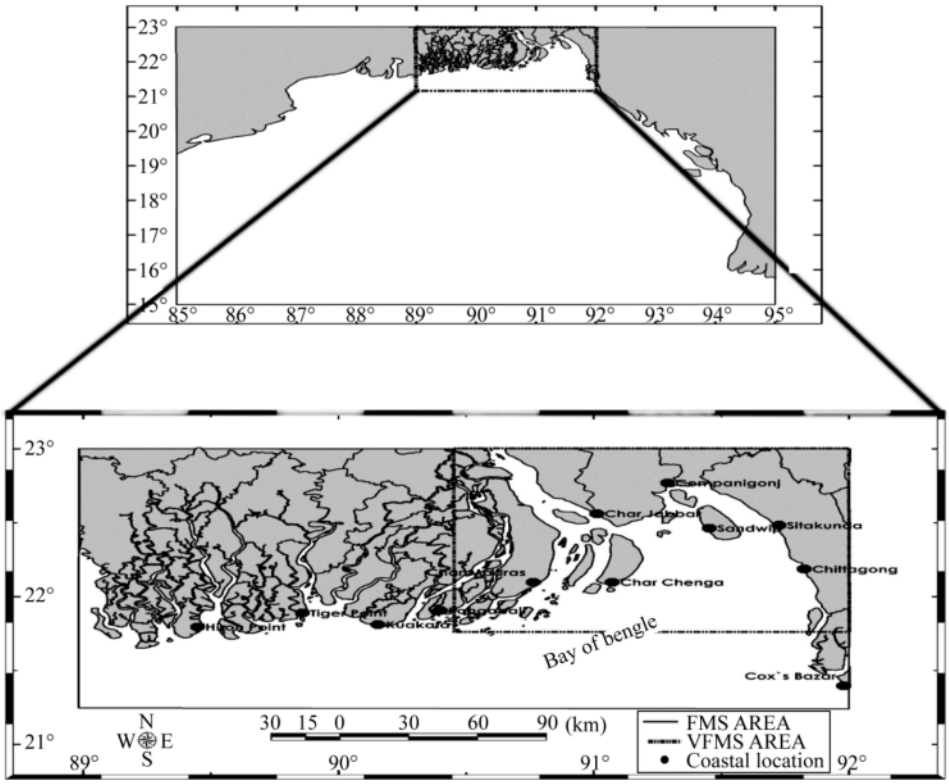

Fig. 1. Study area with the specifications of the regions of CMS, FMS and VFMS (after Paul et al., 2014).

Table 1 Domains, grid resolutions and number of grid points of different schemes

Model	Domain	Grid resolution along x-axis	Grid resolution along y-axis	Number of grid points
CMS	15°–23° N and 85°–95° E	15.08 km	17.52 km	60×61
FMS	21.25°–23° N and 89°–92° E	2.15 km	3.29 km	92×95
VFMS	21.77°–23° N and 90.40°–92° E	720.73 m	1142.39 m	190×145

schemes is important. The same procedure of coupling is adopted here which can be found in the investigation of Rahman et al. (2017).

3.2 Grid generation

The governing equations prescribed by Eqs. (1)–(3) as well as the boundary conditions specified by Eqs. (9)–(11) are discretized by considering a set of grid points defined by

$x_i = (i-1)\Delta x,\ i = 1, 2, 3, ..., m,$

$y_i = (j-1)\Delta y,\ j = 1, 2, 3, ..., n.$

It is found in the investigation due to Ali (1979) that an un-staggered grid cannot handle high frequency waves, particularly two grid waves properly. Therefore, bearing this idea in mind, we have used the staggered Arakawa C-grid shown in Fig. 2. In this grid structure, momentum and scalar variables are stored at dissimilar grid points. If a grid point is (even, odd), i.e., if i and j are even and odd, respectively, the grid point is designated as a ζ-point at which ζ is computed. If a grid point is (odd, odd), it is a u-point at which u is computed and finally, if a grid point is (even, even), it is a v-point, at which v is computed. We select m, the number of grid points along x- axis, to be even, then with this selection, the open sea boundary lying parallel to

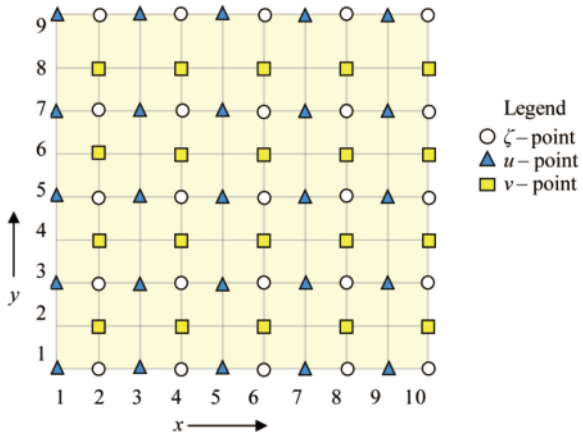

Fig. 2. Arakawa C-grid used in the study.

y-axis consists of ζ and v-points. Furthermore, we choose n, the number of grid points along y- axis, to be odd, then the open boundaries along and parallel to x-axis contain ζ- and u-points (see Fig. 2). Since the computation technique deals with a rectangular grid, the land-sea interfaces are rectangularized by applying stair step method. A detail of the approximation procedure through stair step method can be found in Murshed et al. (2016). Grids of the FMS and VFMS and approximated coastal and island boundaries obtained through stair step representation as well as an enlarged view of a portion of each of the schemes is presented in Fig. 3 for clear understanding, from which one can see how much closely the coastal complexities are solved in the VFMS.

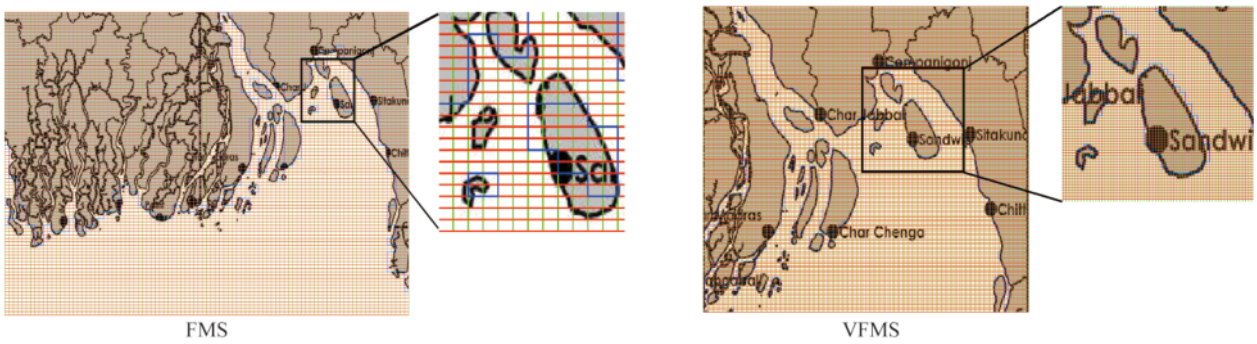

FMS VFMS

Fig. 3. Grids of the FMS and VFMS and approximated coastal and island boundaries obtained though stair step representation with an enlarged view at the right of the selected same portion of each scheme.

3.3 Discretization of spatial derivatives

The governing equations specified by Eqs. (1)–(3) are discretized by applying a 3-point centered finite difference in space to the partial derivatives on an Arakawa C-grid shown in Fig. 2. Thus, when the discretizations are made, a system of first order ODEs with time as an independent variable at every grid point (x_i, y_j) is obtained (see Appendix). The system of ODEs presented in the Appendix is similar to those obtained in Paul et al. (2014, 2018a, 2018b), but as a result of adding the tide generating forcing term and inverse barometer, there is a difference. Therefore, to have subsequent related advantages, the system of ODEs with a description of each term is presented in the Appendix.

3.4 Solution by the RK(4, 4) method

At the points (x_i, y_j), where $i = 2, 4, \ldots, M-2$ and $j = 3, 5, \ldots, N-2$, Eq. (i) in the Appendix can be put into the form (see Appendix):

$$\left(\frac{\partial \zeta}{\partial t}\right)_{i,j} = f_1\left(\zeta^k_{l,m}, u^k_{l,m}, v^k_{l,m}, h_{l,m}\right), \tag{16}$$

where $l = i-1,\ i,\ i+1$; $m = j-1,\ j,\ j+1$.

Similarly, at the grid points (x_i, y_j) with $i = 3, 5, \ldots, M-1$ and $j = 3, 5, \ldots, N-2$, Eq. (ii) in the Appendix can be set to the form:

$$\left(\frac{\partial u}{\partial t}\right)_{i,j} = f_2\left(\zeta^{k+1}_{l,m}, u^k_{l,m}, v^k_{l,m}, h_{l,m}\right), \tag{17}$$

where $l = i-2, i-1, i, i+1, i+2$ and $m = j-2,\ j-1,\ j,\ j+1,\ j+2$.

To the end, at the grid points (x_i, y_j) with $i = 2, 4, \ldots, M-2$ and $j = 2, 4, \ldots, N-1$, one can set Eq. (iii) in the Appendix as:

$$\left(\frac{\partial v}{\partial t}\right)_{i,j} = f_3\left(\zeta^{k+1}_{l,m}, u^k_{l,m}, v^k_{l,m}, h_{l,m}\right), \tag{18}$$

where $l = i-2,\ i-1,\ i,\ i+1,\ i+2$; $m = j-2,\ j-1,\ j,\ j+1,\ j+2$.

In the above system of differential equations specified by Eqs. (13)–(15), the superscripts k and $k+1$ specify the values at the k-th and $k+1$-th time levels, respectively. The acquainted values of $\zeta^k_{l,m}$, $\zeta^{k+1}_{l,m}$, $u^k_{l,m}$, $v^k_{l,m}$ and $h_{l,m}$ in Eqs. (16)–(18) are supplied as initial conditions (ICs) for solving the system of ODEs given by Eqs. (16)–(18) at each time instant.

First, Eq. (13) with the necessary starting values mentioned above is computed by means of the RK(4, 4) method, which in turn can be set to the following form:

$$\zeta^{k+1}_{i,j} = \zeta^k_{i,j} + (k_1 + 2k_2 + 2k_3 + k_4)/6. \tag{19}$$

It is to be mentioned here that the simulations are made with our developed program in MATLAB 18.

In the above equation, the slopes, k_1, k_2, k_3 and k_4 are given by

$$k_1 = \Delta t\, f_1\left(\zeta^k_{l,m},\ u^k_{l,m},\ v^k_{l,m},\ h_{l,m}\right);$$

$$k_2 = \Delta t\, f_1\left(\zeta^k_{l,m} + \frac{1}{2}k_1,\ u^k_{l,m},\ v^k_{l,m},\ h_{l,m}\right);$$

$$k_3 = \Delta t\, f_1\left(\zeta^k_{l,m} + \frac{1}{2}k_2,\ u^k_{l,m},\ v^k_{l,m},\ h_{l,m}\right);$$

$k_4 = \Delta t\, f_1\left(\zeta^k_{l,m} + k_3,\ u^k_{l,m},\ v^k_{l,m},\ h_{l,m}\right)$,

where $l = i-1,\ i,\ i+1$ and $m = j-1,\ j,\ j+1$.

After computing ζ at the grid points specified by Eq. (16), Eqs. (iv)–(vi) in the Appendix are employed to update ζ at the grid points on the model boundaries. Weighted averaged procedure is taken into account to obtain ζ at the remaining points representing water. The path of the cyclone with the required meteorological information is presented in Table 2. The wind and pressure fields are subsequently generated with the help of Eqs. (12) and (13), respectively. Eq. (17) is then taken into account to solve u with the RK(4, 4) method, which is not detailed here, as the solution procedure is similar to that of Eq. (16). Finally, Eq. (18) is solved in a similar manner for y component of velocity. The solution procedure of the system of equations specified by Eqs. (16)–(18) can be found in detail in Paul et al. (2018b). However, the procedure mentioned above is implemented for all the schemes with different open boundary conditions for different schemes. The CMS is independent, which is run with the prescribed boundary conditions. Then the FMS is run having the boundary conditions from the CMS. The process adopted here for specifying the variables, scalar and momentum, by the CMS to the open boundaries of the FMS can be found in detail in the investigations of Paul et al. (2014, 2018a, 2018b) and Rahman et al. (2017). In a similar way, VFMS is run with the boundary information from the FMS. The process mentioned above is maintained for the specified time (59 h: 0900 UTC 23 May–2000 UTC 25 May) with suitable time step using updated values of the variables as that of initial ones.

3.5 Data sources, model data set up and model run

We have procured meteorological inputs, namely time variation positions of the storm, the central pressures, maximum sustained wind, and maximum sustained wind radius (R) from the BMD for the cyclone AILA as our numerical experiments are made with that storm. Sea bed depth from the MSL at our model desired points are compiled from the British Admiralty chart using Shepard interpolation formula with power parameter 2. A detail of it can be found in Paul et al. (2017). Observed water levels are obtained from BIWTA (Bangladesh Inland Water Transport Authority). For friction coefficient C_f, we set the generally accepted value of 0.0026. It is to be noted here that the value of C_f may be changed depending on the bottom condition and the non-linear bottom friction introduces an interaction between tide and surge that has an important influence on sea-level variations (Murty and Greenberg, 1987).

In our numerical experimentations, first, tide model is run. To produce a stable tidal condition in the region of interest, the sea level was forced to be oscillatory with the M_2 tidal constituent along the southern open boundary of the outermost scheme (CMS) in the absence of atmospheric pressure gradient force, wind stress and TGFs. The values of the constants associated with the M_2 tidal constituents are taken from the study of Paul et al. (2018b) as $a = 0.3$ m and $\phi = 0$ and following a process detailed in the study of Roy (1995), a stable tidal condition is generated. It is mentioned at this juncture that the initial conditions, i.e., the values of ζ, u and v are initially set to zero, known as cold start. The effect of such cold start on the computed results over several hours almost dies out (Zhang et al., 2007). The choice of the minimum grid resolution with maximum water depth allowed to take the time step as 30 s that ensured CFL stability criterion. When the tidally forced water level is in its stable condition, then the surge model is run with $t = 0$ introducing inverse barometer, wind stress and TGFs for nonlinear interaction of tide and surge. The surge model that results from atmospheric pressure gradient force, wind stress and TGFs in the absence of astronomical tide is also computed from the cold start to foresee water levels due to surge only, referred to as pure surge. The computed results that came out through simulations are depicted at some of

Table 2 Time variation positions, central pressures, maximum sustained surface wind and the nature of the cyclone AILA over the BOB during 23–25 May 2009 (Source: BMD, IMD)

Date	Hour (UTC)	Latitude (°N)	Longitude (°E)	Central pressure (hPa)	Maximum surface wind (kt)	Nature of the storm
23 May	0900	16.00	88.00	998	25	Depression
23 May	1500	16.50	88.00	996	25	Depression
24 May	0000	17.20	88.30	996	25	Depression
24 May	0600	17.80	88.60	994	30	Deep depression
24 May	0900	17.80	88.60	994	30	Deep depression
24 May	1200	18.30	88.60	994	35	Cyclonic storm
24 May	1800	18.80	88.60	990	35	Cyclonic storm
24 May	2100	19.20	88.60	987	40	Cyclonic storm
25 May	0000	19.40	88.60	987	40	Cyclonic storm
25 May	0300	20.00	88.60	987	50	Cyclonic storm
25 May	0600	21.60	88.30	987	55	Cyclonic storm
25 May	1200	22.90	88.30	970	50	Cyclonic storm
25 May	2000	24.20	88.50	980	40	Cyclonic storm

Maximum wind speed: 120 km/h, maximum radius of sustained wind: 54 km

the positions shown in Fig. 1. Our numerical experimentations are performed for 59 h from 0900 UTC 23 May to 2000 UTC 25 May and the results are presented for the last 2 days. For analysis of the model simulated results, its synoptic history is of importance. A detailed history in this regard can be found in Paul et al. (2016), but for better understanding, the time variation positions, central pressure, maximum sustained surface wind and the nature of the cyclonic storm, AILA are presented in Fig. 4 and tabulated in Table 2 for better perspective.

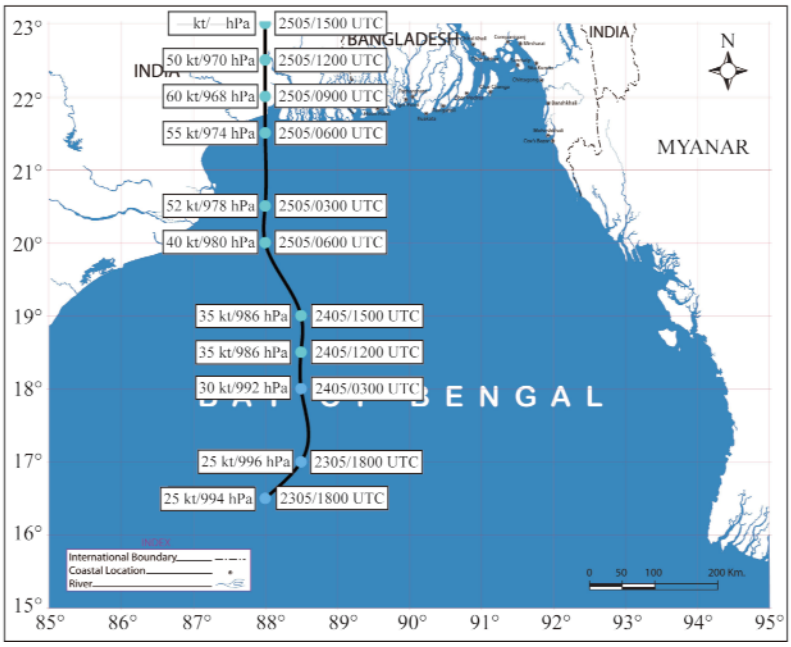

Fig. 4. Observed track, and intensity of the cyclonic storm AILA, 2009, according to the Saffir–Simpson scale, as well as the central pressure information (Data source: BMD and IMD). The numbers in the left such as 25 kt/994 hPa mean the storm intensity is 25 kt and central pressure is 994 hPa and the numbers in the right such as 2305/1200 UTC mean the time is 1200 UTC of 23 May.

4 Results discussion and model validation

4.1 Results and validation

Fig. 5 displays our model simulated water levels due to tide in the absence of atmospheric pressure gradient force, wind stress and TGFs at Hiron Point and Chittagong. Fig. 5 also includes temporal variation of water levels due to tide in the presence of TGFs. The reason behind the choice of the places is the obtainability of tidal information. Our simulated results due to tide with TGFs at these places are in a reasonable agreement with the tidal elevation data obtained from BIWTA (Fig. 5), which can also be found to be consistent with those presented in Paul et al. (2016). The observations in this regard can be found in subsection 5.2.

Fig. 6 depicts the temporal variation of our simulated water levels due to surge without the contribution of astronomical tide at some representative stations shown in Fig. 1, from which it is seen that our simulated peak water levels due to surge vary between 1.29 m (Kuakata) and 2.89 m (Companigonj). Paul et al. (2018b) in their investigation estimated 1.82–3.71 m surge in the absence of astronomical tide, whereas Rahman et al. (2011) found them to range between 1.40 m and 2.95 m along the area of interest. According to a report from the Goddard Space Flight of National Aeronautics and Space Administration (NASA), a storm surge of 3.05–3.96 m was found to occur along the

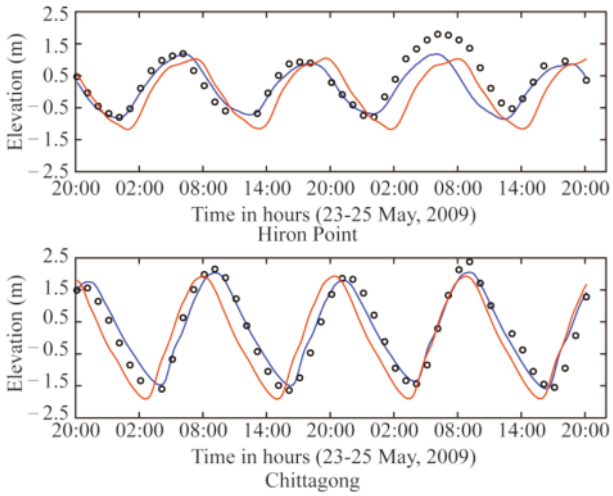

Fig. 5. Computed temporal variation tidal levels with respect to the mean sea level (MSL) at Hiron Point and Chittagong with the tidal data obtained from BIWTA. In each case, a solid blue curve represents our computed tidal results with tide generating forces, a solid red curve for that without tide generating forces and a circle represents the data obtained from BIWTA (whenever available).

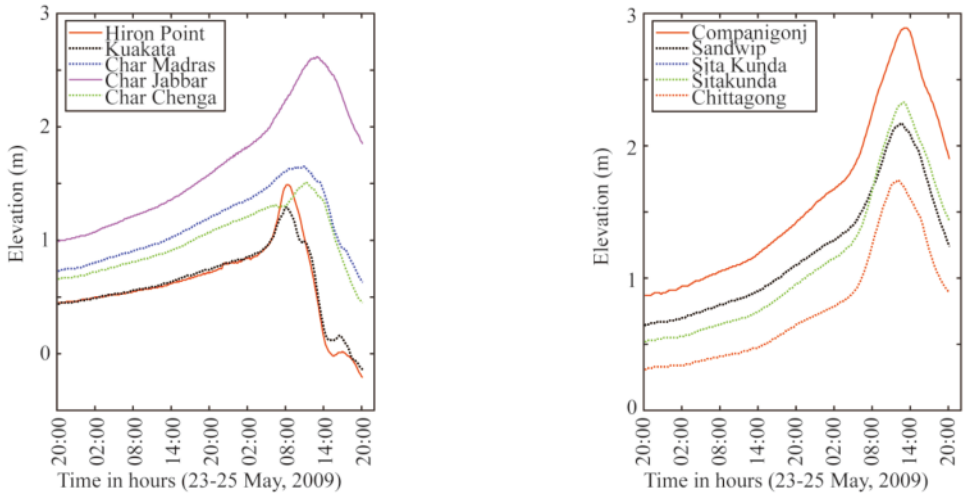

Fig. 6. Temporal variation of water levels with respect to the MSL due to the pure surge resulted from wind stress forcing, inverse barometer and TGFs associated with the storm AILA along the coast of Bangladesh.

western Bangladesh coastline at the time of landfall. Further, based on a report from Indian Meteorological Department (IMD), about 2–3 m high storm surge above the astronomical tide was realized along the West Bengal and neighboring Bangladesh coasts. Thus, the peak surge (pure) values that came out through our model simulation are found to be in a reasonable agreement with some reported data and with the results obtained in Rahman et al. (2011) and Paul et al. (2016, 2018b).

Our computed temporal variation of water levels as a result of interacting surge with tide at some coastal locations are displayed in Fig. 7. The peak water levels due to the dynamical interaction of tide and surge, referred to as total water levels, can be found to range from 2.75 to 5.02 m. Paul et al. (2016) estimated 3.30–5.97 m water levels due to the interaction of tide and surge along the area of interest. In their investigation, Paul et al. (2018b) simulated 2.63–5.62 m high total water levels along this region. As in Roy et al. (2009), the total water level associated with the storm AILA at the time of landfall was 4–5 m. According to BMD, AILA made landfall between 0800 and 0900 UTC of 25 May over Bangladesh coast (Khulna) when the local astronomical tide was at peak. Our estimated results displayed in Fig. 7 are found to be consistent with the sequence of events and total water levels obtained in some investigations and reported data.

For model validation, we present our model simulated temporal variation of total water levels at Hiron Point, Char Chenga, and Chittagong with observed data procured from BIWTA for the mentioned period in Fig. 8. Fig. 8 also includes total water levels that result from using the FDM. The procedure for the FDM is available in detail in our investigation (see Rahman et al., 2017). However, it can be perceived from Fig. 8 that our simulated temporal variation of total water levels compares reasonably well with the observed data from BIWTA and with the ones obtained by the

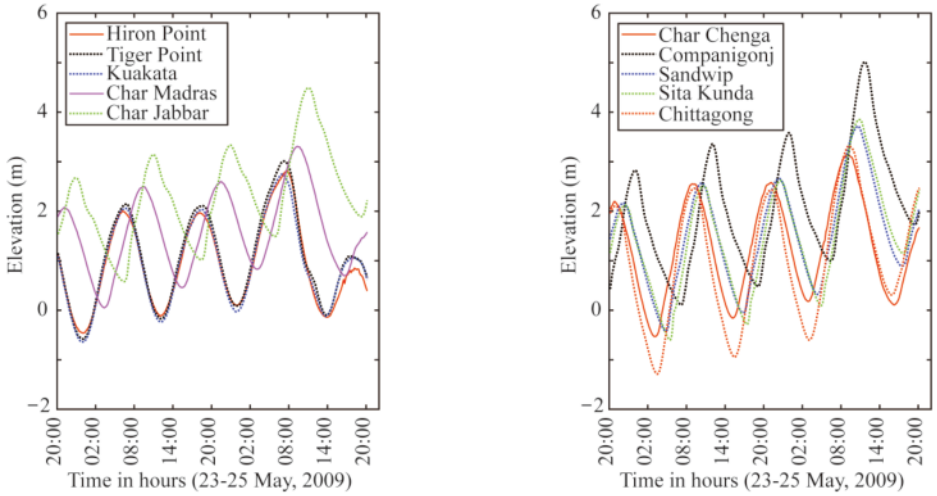

Fig. 7. Temporal variation of water levels with respect to the MSL due to the dynamical interaction of tide and surge associated with the storm AILA along the coast of Bangladesh.

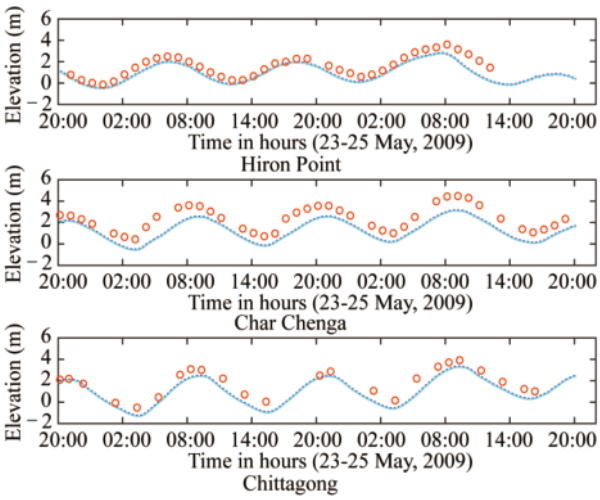

Fig. 8. Comparison of temporal variation of total water levels simulated by the present study and FDM with observed data. In each figure, a dotted blue curve represents our computed temporal variation of total water levels due to the interaction of tide and surge by the MOLs, a solid cyan curve represents that obtained with the FDM and a circle with red color represents the observed data (whenever available).

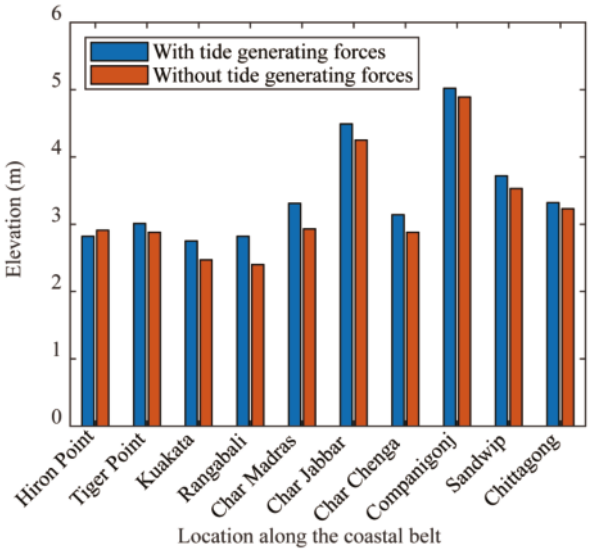

Fig. 9. Computed maximum total water levels with respect to the MSL due to the storm AILA along the coast of Bangladesh.

FDM. By reason of paucity of authentic observed data at the remaining locations, our comparison with observed data is confined only at the above-mentioned positions. However, the results for temporal variation of total water levels at the remaining locations compare well with those obtained by using the FDM. But due to the sake of brevity, they are not presented.

4.2 Effect of tide generating forces

To obtain the impact of TGFs on water levels due to astronomical tide, we calculated water levels due to tide with and without TGFs devoid of the meteorological forcing terms in both cases and are presented in Fig. 5. It can be inferred from Fig. 5 that there is a change in amplitude and phase if the TGFs are not taken into account. The results that came out including TGFs agree with the BIWTA data better over the tidal results emanated without using TGFs. Thus, it is suggestive to predict correctly the tidal phase and amplitude, TGFs should be included as body forces. We have also tested the effect of TGFs on computing water levels as a result of tide surge interaction (TSI). Our computed results in this respect are presented in Fig. 9 from which it is seen that the peak value of total water level at every location except Hiron Point increases while TGFs are taken into consideration. It is mentioned here that Hiron Point is situated outside the region where the VFMS is exercised. Total water levels along the Meghana estuary are found to be influenced more by TGFs over the other places along the Bangladesh coast, though AILA crossed over the western parts of Bangladesh, which strongly supports the results obtained in Rahman et al. (2017). The reasons behind the fact may be the geographical location of the Meghana estuary, its funnel shaped coast with complex domain, shallow bathymetry, thickly populated island, etc. Thus, based on the obtained results, it is reasonable to note here that the head of the northern part of the BOB is a region, where water levels are influenced by TGFs. Therefore, it is evocative that for accurate prediction of peak water levels associated with a cyclone for the region of our consideration, TGFs should be taken carefully into account.

4.3 Tide surge interaction

The impact of tide surge interaction (TSI) in the BOB was studied by several authors. Some worth mentioning works are those of Johns and Ali (1980), Murty et al. (1986), and As-Salek and Yasuda (2001). However, the study of TSI including TGFs has received limited attention. The interaction effect can be assessed by taking into account the temporal variation of water levels due to astronomical tide only (in the absence of atmospheric forcing) at a fixed location, surge only (in the absence of astronomical tide) and simultaneous presence of both tide and surge (see Johns and Ali, 1980). By denoting these quantities by ζ_T, ζ_S, and $\zeta_{T+S+IST}$, respectively, it is suitable to express the elevation owing to the interaction effect between tide and surge by $\zeta_{S+IST} = \zeta_{T+S+IST} - \zeta_T$ (Johns and Ali, 1980), which is termed as non-tidal residual. We have estimated the interactive effect at two points, namely Hiron Point and Chittagong (see Fig. 10). The figure depicts the time-based variation of ζ_T, ζ_S, $\zeta_{T+S+IST}$ and ζ_{S+IST}. It can be seen from the figure that the elevation due to ζ_{S+IST} is higher than that of ζ_S at times of low tide at both the stations, Hiron Point and Chittagong. Therefore, there is a difference between non-tidal residual with that of the surge that results from meteorological forcing in the absence of astronomical tide. Thus, non-tidal residual can be affected by TSI. It can also be in-

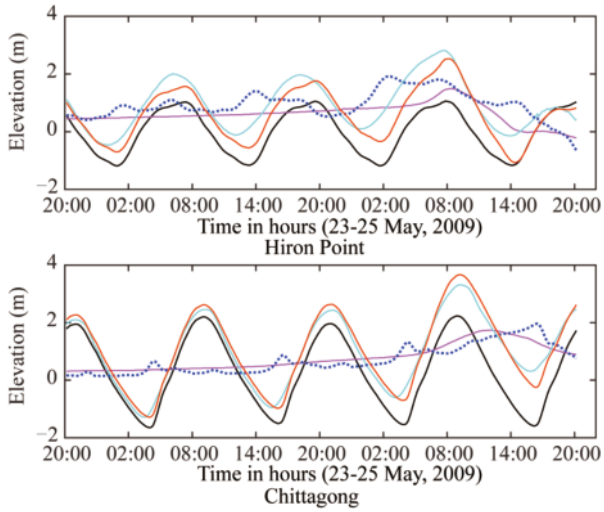

Fig. 10. Temporal variation of water levels at Hiron Point, and Chittagong. In each figure, a solid black curve represents the configuration for tide (ζ_T), a solid magenta curve for surge (ζ_S) (in the absence of astronomical tide), a solid cyan curve for interaction of tide and surge ($\zeta_{S+T+IST}$), a dotted blue curve for interaction effect (ζ_{S+IST}) and a solid red curve for superposition of tide and surge (ζ_{S+T}).

ferred from Fig. 10 that the peak values of $\zeta_{T+S+IST}$ consistently occur after the time of high tide. The above characteristics can be found to be consistent with those found in the study of Johns and Ali (1980). Fig. 10 also includes the elevation of water levels that came out through superposition of surge with tide ($\zeta_{S+T} = \zeta_S + \zeta_T$). It can be inferred in the case of superposition that both magnitude and phase of the obtained results differ with those resulted from TSI. Thus the interaction of tide and surge should be taken into account very carefully, which can affect the timing of extreme elevations of water levels during cyclonic events, which in turn can lead to better estimates of extreme elevation of water levels on time in coastal defense.

4.4 Skew surge

We have estimated skew surges at the three stations with the maximum peaks at Hiron Point, Char Chenga and Chittagong as 2.55 m, 2.53 m and 1.69 m, respectively. We estimated skew surges at those stations because of the availability of observed data. The advantage of skew surge, the difference between the maximum observed water level and the maximum predicted tidal level regardless of their timing during the tidal cycle, is that it contains the true meteorological contribution to the surge. The skew surge is usually a more useful metric to predictors than non-tidal residual, ζ_{S+IST} (see Fig. 11) (Williams et al., 2016), because with this amount, the highest water level will exceed the expected maximum water level that is most significant in terms of flooding.

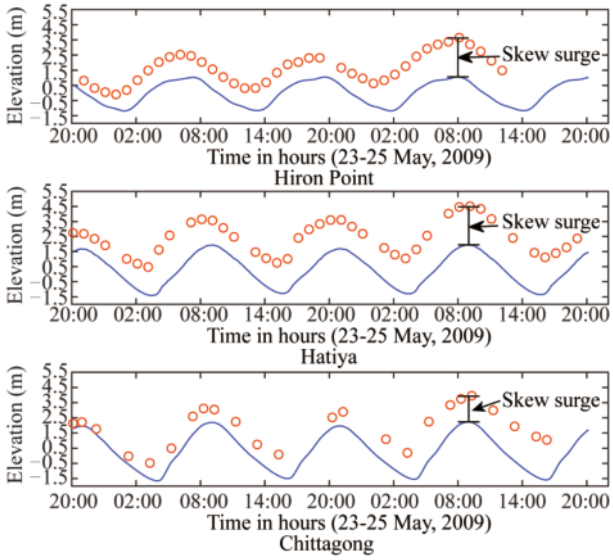

Fig. 11. Skew surges at three stations, namely Hiron Point, Hatiya and Chittagong.

4.5 Model performance

To examine our hydrodynamic model performance and to make comparison with that of the FDM, the root mean square errors (RMSEs) were estimated amongst the computed total water levels yielded by both the models and observed data from BIWTA for the period mentioned above. The expression for RMSE is $RMSE=\sqrt{\frac{1}{N}\sum_{i=1}^{N}(X_{\mathrm{obs},i}-X_{\mathrm{model},i})^2}$, where $X_{\mathrm{obs},i}$ is the observed value and $X_{\mathrm{model},i}$ is the modelled result at time i and N represents the size of the sample. Table 3 shows our estimated RMSEs form which it can be perceived that our model performance is satisfactory and better over the FDM. We have likewise evaluated RMSEs to see the impacts of each of the factors, namely TGFs, offshore islands, inverse barometer (IB) and grid resolution on our model simulated total water levels. In doing so, the RMSEs are calculated between the observed data and the estimated total water levels from the model run in each case without the function of TGFs, IB, islands, and without that of VFMS. The corresponding RMSE values are inserted in the same table (Table 3). It is inferred from Table 3 that the

Table 3 Estimated root mean square errors in metre. The errors have been estimated between the computed and observed water levels from 2000 UTC May 23 to 2000 UTC May 25. We used all the observed data whenever available in the mentioned period

Coastal station	Estimated by the present study	Estimated by the FDM	Without islands	Without TGFs	Without VFMS	Inverse barometer
Hiron Point	0.64	0.67	0.66	0.69	0.64	0.80
Char Chenga	0.83	0.86	0.87	0.88	0.85	0.98
Chittagong	0.72	0.76	0.80	0.75	0.82	0.92

impact of each of the factors, namely TGFs, IB, offshore islands, and grid resolution on estimating water level associated with a storm for the region of our choice can no longer be overlooked.

4.6 Computational efficiency

In our numerical experimentations, a time step of 30 s is used. Though, we have depicted the model simulated results with time step as 30 s, nonetheless, we have also carried out experiments with time steps of 90 s, 60 s, 30 s, 20 s and 10 s. The results obtained employing the MOLs for each of the time steps, in general, supported the depicted results and no numerical instability was attained. However, the FDM was found to be unsuccessful with regard to stability for some of the mentioned time steps. We have tested computational efficiency of the MOLs and FDM. In order to do it, both the codes for the MOLs and FDM were run on the same PC in computing water levels due to surge, tide and interaction of tide and surge with time step of 30 s. The comparison indicates that the MOLs solutions are more efficient with respect to CPU time over the FDM solutions.

4.7 Model limitations and future openings

The results obtained in the study might be changed as there are some rivers, which provide additional paths to the storm surge water to release into the rivers, instead of getting piled up. These studies are in progress and will be reported in future papers.

In our study, we have used fixed value ($H_0 = 2$) for the Holland's radial pressure profile parameter H_0, but we have tested its possible variation on estimating total water levels. The obtained water levels in this regard were found to generally support the results presented through graphical outputs.

In our model, we used the maximum sustained wind radius (R) from BMD. It is mentionable here that R is one of the important parameters for accurate estimation of storm surges (Takagi and Wu, 2016). The winds near the core of a storm most significantly impact the generation of maximum storm surges, whereas the winds at larger radii also play a significant role (Mayo and Lin, 2019). According to Jordan (1961), the storm eye usually decreases in size as the storm deepens with the minimum value occurring near the time of lowest pressure, R decreases logarithmically with the central pressure depth (Fujii, 1998). Loder et al. (2009) studied various physical factors influencing peak surge elevation for an idealized marsh and confirmed that the difference in R of 3.7 times causes a difference of 40 % in the simulated surge height. Thus, an exploration in this regard is of importance, which is out of the scope of the study, but it can be a part of future study.

In our numerical work, we assume a fixed value of C_f in the absence of any empirical model for it. Such a consideration is supported by several investigations (Roy et al., 1999; Paul et al., 2016, 2018a; Rahman et al., 2017). However, increased bottom friction resulted from continuous erosion and sedimentation of coastal areas and wetlands due to frequent storm surges, waves and winds along the region of interest may change the result as it came out through this investigation. It can be noted down here that the increased bottom friction causes decreased water elevation due to the increase in energy dissipation at the sea floor (Akbar et al., 2017), while a lower bottom friction causes higher and faster surge propagation, which in turn may cause earlier peak arrival than cases with higher friction (Akbar et al., 2017). A correct bottom friction based on actual sea floor material may be a solution in this regard. These studies are in progress and would be reported in future papers.

5 Conclusions

In this study, we have simulated storm surges including TGFs. The MOLs in addition to well-established RK(4, 4) technique has been applied for solving SWEs to foresee water levels due to the dynamical interaction of tide and surge along the coast of Bangladesh efficiently. One-way grid nesting is exercised to solve coastal complexities easily and economically. The model simulated results are found to be satisfactory with observation and are found to be better over those resulted from using the FDM with regard to CPU time, numerical stability and accuracy. Though there is a limitation of essential data (e.g., observed temporal variation of water level data, accurate water depth data, etc.), an effort is given to make the study reliable and meaningful through proper utilization of available authentic data. Thus the study can be of importance to rectify tidal level as well as to include near-shore coastal complexities with minimum cost which are desirable for accurate forecasting of water levels.

Acknowledgments

We are grateful to the anonymous three referees for valuable comments and appreciated suggestions that helped improve this manuscript. The authors also would like to thank Mr. Md. Mahabub Alam, an M.Sc. thesis student, for providing necessary data and helping us in designing a figure (Fig. 4).

References

Akbar, M.K., Kanjanda, S. and Musinguzi, A., 2017. Effect of bottom friction, wind drag coefficient, and meteorological forcing in hindcast of hurricane Rita storm surge using SWAN+ADCIRC model, *Journal of Marine Science and Engineering*, 5(3), 38.

Ali, A., 1979. *Storm Surges in the Bay of Bengal and Some Related Problems*, Ph.D. Thesis, University of Reading, England.

As-Salek, J.A. and Yasuda, T., 2001. Tide-surge interaction in the Meghna Estuary: Most severe conditions, *Journal of Physical Oceanography*, 31(10), 3059–3072.

Das, P.K., 1994. On the prediction of storm surges, *Sadhana*, 19(4), 583–595.

Debsarma, S.K., 2009. Simulations of storm surges in the Bay of

Bengal, *Marine Geodesy*, 32(2), 178–198.

Erşahin, C., Tarhan, T., Tuncer, I.H. and Selçuk, N., 2004. Parallelization of a transient method of lines Navier–Stokes code, *International Journal of Computational Fluid Dynamics*, 18(1), 81–92.

Fujii, T.K., 1998. Statistical analysis of the characteristics of severe typhoons hitting the Japanese main islands, *Monthly Weather Review*, 126(4), 1091–1097.

Holland, G.J., 1980. An analytic model of the wind and pressure profiles in hurricanes, *Monthly Weather Review*, 108(8), 1212–1218.

Ismail, A.I.M., Karim, F., Roy, G.D. and Meah, M.A., 2007. Numerical modelling of tsunami via the method of lines, *Proceedings of World Academy of Science, Engineering and Technology*, 36, 177–185.

Jelesnianski, C.P., 1965. A numerical calculation of storm tides induced by a tropical storm impinging on a continental shelf, *Monthly Weather Review*, 93(6), 343–358.

Johns, B. and Ali, M.A., 1980. The numerical modelling of storm surges in the Bay of Bengal, *Quarterly Journal of the Royal Meteorological Society*, 106(447), 1–18.

Jordan, C.L., 1961. Marked changes in the characteristics of the eye of intense typhoons between the deepening and filling stages, *Journal of Meteorology*, 18(6), 779–789.

Loder, N.M., Cialone, M.A., Irish, J.L. and Wamsley, T.V., 2009. *Idealized Marsh Simulations: Sensitivity of Storm Surge Elevation to Seabed Elevation*, Coastal and Hydraulics Engineering Technical Note ERDC/CHL CHETN-I-78, U.S. Army Engineer Research and Development Center, Vicksburg, MS.

Loy, K.C., Sinha, P.C., Liew, J., Tangan, F. and Husain, M.L., 2014. Modeling storm surges associated with super typhoon durian in South China Sea, *Natural Hazards*, 70(1), 23–37.

Mayo, T. and Lin, N., 2019. The effect of the surface wind field representation in the operational storm surge model of the national hurricane center, *Atmosphere*, 10(4), 193.

Murshed, M.M., Paul, G.C. and Haque, M.R., 2016. On the approximation of complex geometric domain to be compatible for the implementation of finite difference method, *International Journal of Scientific & Engineering Research*, 7(5), 495–501.

Murty, T.S., Flather, R.A. and Henry, R.F., 1986. The storm surge problem in the Bay of Bengal, *Progress in Oceanography*, 16(4), 195–233.

Murty, T.S. and Greenberg, D.A., 1987. Numerical simulation of the storm surge of January 1982 on the south coast of Newfoundland, *Atmosphere-Ocean*, 25(1), 46–59.

Oymak, O. and Selçuk, N., 1993. MOL vs FDM solutions of an unsteady viscous flow problem, *Proceedings of the 8th International Conference on Numerical Methods in Laminar and Turbulent Flows*, Swansea, 153–162.

Paul, G.C. and Ismail, A.I.M., 2012. Tide-surge interaction model including air bubble effects for the coast of Bangladesh, *Journal of the Franklin Institute*, 349(8), 2530–2546.

Paul, G.C. and Ismail, A.I.M., 2013. Contribution of offshore islands in the prediction of water levels due to tide-surge interaction for the coastal region of Bangladesh, *Natural Hazards*, 65(1), 13–25.

Paul, G.C., Ismail, A.I.M. and Karim, M.F., 2014. Implementation of method of lines to predict water levels due to a storm along the coastal region of Bangladesh, *Journal of Oceanography*, 70(3), 199–210.

Paul, G.C., Ismail, A.I.M., Rahman, A., Karim, M.F. and Hoque, A., 2016. Development of tide-surge interaction model for the coastal region of Bangladesh, *Estuaries and Coasts*, 39(6), 1582–1599.

Paul, G.C., Murshed, M.M., Haque, M.R., Rahman, M.M. and Hoque, A., 2017. Development of a cylindrical polar coordinates shallow water storm surge model for the coast of Bangladesh, *Journal of Coastal Conservation*, 21(6), 951–966.

Paul, G.C., Senthilkumar, S. and Pria, R., 2018a. Storm surge simulation along the Meghna estuarine area: An alternative approach, *Acta Oceanologica Sinica*, 37(1), 40–49.

Paul, G.C., Senthilkumar, S. and Pria, R., 2018b. An efficient approach to forecast water levels owing to the interaction of tide and surge associated with a storm along the coast of Bangladesh, *Ocean Engineering*, 148, 516–529.

Powell, M.D., Vickery, P.J. and Reinhold, T.A., 2003. Reduced drag coefficient for high wind speeds in tropical cyclones, *Nature*, 422(6929), 279–283.

Pugh, D.T., 1987. *Tides, Surges, and Mean Sea-Level*, John Wiley & Sons, New York.

Rahman, M.M., Paul, G.C. and Hoque, A., 2011. A shallow water model for the coast of Bangladesh and applied to estimate water levels for 'AILA', *Journal of Applied Sciences*, 11(24), 3821–3829.

Rahman, M.M., Paul, G.C. and Hoque, A., 2013. Nested numerical scheme in a polar coordinate shallow water model for the coast of Bangladesh, *Journal of Coastal Conservation*, 17(1), 37–47.

Rahman, M.M., Paul, G.C. and Hoque, A., 2017. A shallow water model for computing water level due to tide and surge along the coast of Bangladesh using nested numerical schemes, *Mathematics and Computers in Simulation*, 132, 257–276.

Roy, G.D., 1995. Estimation of expected maximum possible water level along the Meghna estuary using a tide and surge interaction model, *Environment International*, 21(5), 671–677.

Roy, G.D., Kabir, A.B.M.H., Mandal, M.M. and Haque, M.Z., 1999. Polar coordinates shallow water storm surge model for the coast of Bangladesh, *Dynamics of Atmospheres and Oceans*, 29(2–4), 397–413.

Roy, K., Kumar, U., Mehedi, H., Sultana, T. and Ershad, D.M., 2009. *Initial Damage Assessment Report of Cyclone Aila with Focus on Khulna District*, Unnayan Onneshan-Humanitywatch-Nijera Kori, Khulna.

Schwiderski, E.W., 1980. On charting global ocean tides, *Reviews of Geophysics*, 18(1), 243–268.

Selçuk, N., Tarhan, T. and Tanrıkulu, S., 2002. Comparison of method of lines and finite difference solutions of 2-D Navier–Stokes equations for transient laminar pipe flow, *International Journal for Numerical Methods in Engineering*, 53(7), 1615–1628.

Takagi, H. and Wu, W.J., 2016. Maximum wind radius estimated by the 50 kt radius: Improvement of storm surge forecasting over the western North Pacific, *Natural Hazards and Earth System Sciences*, 16(3), 705–717.

Vatvani, D.K., Goodchild, S., Stelling, G.S., Gerritsen, H., van Holland, G., Hulsen, L., van der Kaaij, T. and Rao, A.V.P.K., 2000. Storm surge models for Bay of Bengal–India and Vietnam, *Proceedings of the RTC Conference on TC and Storm Surges*, Chiang Mai, Thailand.

Vickery, P.J., Skerlj, P.F., Steckley, A.C. and Twisdale, L.A., 2000. Hurricane wind field model for use in hurricane simulations, *Journal of Structural Engineering*, 126(10), 1203–1221.

Williams, J., Horsburgh, K.J., Williams, J.A. and Proctor, R.N.F., 2016. Tide and skew surge independence: New insights for flood risk, *Geophysical Research Letters*, 43(12), 6410–6417.

Zhang, W.Z., Hong, H.S., Shang, S.P., Chen, D.W. and Chai, F., 2007. A two-way nested coupled tide-surge model for the Taiwan Strait, *Continental Shelf Research*, 27(10–11), 1548–1567.

Appendix

For discretization of spatial variables, we use the following notations.

For any dependent variable $\chi(x,y,t)$ at a grid point (x_i,y_j) at time t_k, we use the following notations:

$$\chi\left(x_i,y_j,t_k\right)=\chi_{i,j}^k,\ \frac{1}{2}\left(\chi_{i+1,j}^k+\chi_{i-1,j}^k\right)=\overline{\chi_{i,j}^k}^x,$$

$$\frac{1}{2}\left(\chi_{i,j+1}^k+\chi_{i,j-1}^k\right)=\overline{\chi_{i,j}^k}^y,$$

$$\frac{1}{4}\left(\chi_{i+1,j}^k+\chi_{i-1,j}^k+\chi_{i,j+1}^k+\chi_{i,j-1}^k\right)=\overline{\chi_{i,j}^k}^{xy}.$$

Now, after discretization, Eqs. (1)–(3), following Paul et al. (2014), can be written, respectively, as:

$$\left(\frac{\partial\zeta}{\partial t}\right)_{i,j}=CR1+CR2; \tag{i}$$

where $i=2,\ 4,\ \ldots,M-2$ and $j=3,\ 5,\ \ldots,N-2$.

$$\left(\frac{\partial u}{\partial t}\right)_{i,j}=UR1+UR2+UR3+UR4+UR5+UR6+UR7, \tag{ii}$$

where $i=3,\ 5,\ \ldots,M-1$ and $j=3,\ 5,\ \ldots,N-2$.

$$\left(\frac{\partial v}{\partial t}\right)_{i,j}=VR1+VR2+VR3+VR4+VR5+VR6+VR7, \tag{iii}$$

where $i=2,\ 4,\ \ldots,M-2$ and $j=2,\ 4,\ \ldots,N-1$.

In Eqs. (i)–(iii),

$$CR1=-\frac{\left(\overline{\zeta_{i+1,j}^k}^x+h_{i+1,j}\right)u_{i+1,j}^k-\left(\overline{\zeta_{i-1,j}^k}^x+h_{i-1,j}\right)u_{i-1,j}^k}{2\Delta x},$$

$$CR2=-\frac{\left(\overline{\zeta_{i,j+1}^k}^y+h_{i,j+1}\right)v_{i,j+1}^k-\left(\overline{\zeta_{i,j-1}^k}^y+h_{i,j-1}\right)v_{i,j-1}^k}{2\Delta y},$$

$$UR1=-\begin{cases}u_{i,j}^k\dfrac{u_{i+2,j}^k-u_{i-2,j}^k}{4\Delta x} & \text{for } i\neq M-1\\ u_{i,j}^k\dfrac{0.5(3u_{i,j}^k-u_{i-2,j}^k)-u_{i-2,j}^k}{4\Delta x} & \text{for } i=M-1\end{cases}$$

$$UR2=-\overline{v_{i,j}^k}^{xy}\frac{\overline{u_{i,j+1}^k}^y-\overline{u_{i,j-1}^k}^y}{2\Delta y},$$

$$UR3=f_{i,j}\overline{v_{i,j}^k}^{xy},$$

$$UR4=-g\left(\frac{\zeta_{i+1,j}^{k+1}-\zeta_{i-1,j}^{k+1}}{2\Delta x}-\frac{\eta_{i+1,j}^{k+1}-\eta_{i-1,j}^{k+1}}{2\Delta x}\right),$$

$$UR5=\frac{x_i-x_c}{r_a}\frac{R\Delta p_a H_0}{r_a^2}\exp\left[-(R/r_a)^{H_0}\right],$$

$$UR6=\frac{T_x}{\rho\left(\overline{\zeta_{i,j}^{k+1}}^x+h_{i,j}\right)},$$

$$UR7=-\frac{C_f u_{i,j}^k}{\overline{\zeta_{i,j}^{k+1}}^x+h_{i,j}}\left[\left(u_{i,j}^k\right)^2+\left(\overline{v_{i,j}^k}^{xy}\right)^2\right],$$

$$VR1=-\begin{cases}\overline{u_{i,j}^k}^{xy}\dfrac{\overline{v_{i+1,j}^k}^x-\overline{v_{i-1,j}^k}^x}{2\Delta x}, & \text{for } i\neq 2\\ \overline{u_{i,j}^k}^{xy}\dfrac{\overline{v_{i+1,j}^k}^x-0.5\left(3v_{i,j}^k-v_{i+2,j}^k\right)}{2\Delta x}, & \text{for } i=2\end{cases}$$

$$VR2=-\begin{cases}v_{i,j}^k\dfrac{v_{i,j+2}^k-v_{i,j-2}^k}{4\Delta y}, & \text{for } j\neq 2,\ j\neq N-1\\ v_{i,j}^k\dfrac{v_{i,j+2}^k-0.5\left(3v_{i,j}^k-v_{i,j+2}^k\right)}{4\Delta y}, & \text{for } j=2\\ v_{i,j}^k\dfrac{0.5\left(3v_{i,j}^k-v_{i,j-2}^k\right)-v_{i,j-2}^k}{4\Delta y}, & \text{for } j=N-1\end{cases}$$

$$VR3=-f_{i,j}\overline{u_{i,j}^k}^{xy},$$

$$VR4=-g\left(\frac{\zeta_{i,j+1}^{k+1}-\zeta_{i,j-1}^{k+1}}{2\Delta y}-\frac{\eta_{i,j+1}^{k+1}-\eta_{i,j-1}^{k+1}}{2\Delta y}\right),$$

$$VR5=\frac{y_i-y_c}{r_a}\frac{R\Delta p_a H_0}{r_a^2}\exp\left[-(R/r_a)^{H_0}\right],$$

$$VR6=\frac{T_y}{\rho\left(\overline{\zeta_{i,j}^{k+1}}^x+h_{i,j}\right)},$$

$$VR7=-\frac{C_f v_{i,j}^k}{\overline{\zeta_{i,j}^{k+1}}^x+h_{i,j}}\left[\left(\overline{u_{i,j}^k}^{xy}\right)^2+\left(v_{i,j}^k\right)^2\right]^{1/2}.$$

The boundary conditions, given by Eqs. (9)–(11), are discretized as follows:

For $j=1$, $\zeta_{i,1}^{k+1}=-\zeta_{i,3}^{k+1}-2\sqrt{(h_{i,2}/g)}\,v_{i,2}^k$, (iv)

where $i=2,\ 4,\ 6,\ldots,\ M-2$.

For $j=N$, $\zeta_{i,n}^{k+1}=-\zeta_{i,n-2}^{k+1}+2\sqrt{(h_{i,n-1}/g)}\,v_{i,n-1}^k$, (v)

where $i=2,\ 4,\ 6,\ldots,\ M-2$.

For $i=M$, $\zeta_{m,j}^{k+1}=-\zeta_{m-2,j}^{k+1}+2\sqrt{(h_{m-1,j}/g)}u_{m-1,j}^k+4a\sin\left(\dfrac{2\pi k\cdot\Delta t}{T}+\varphi\right)$, (vi)

where $j=1,\ 3,\ 5,\ 7,\ldots,\ N$.